Imaging Sources with Fast and Slow Emission Components

G. Verde[a] , D.A. Brown[b] , P. Danielewicz[a] , C.K. Gelbke[a] , W.G. Lynch[a] , M.B. Tsang[a]

[a]*National Superconducting Cyclotron Laboratory and the Department of Physics and Astronomy, Michigan State University, East Lansing, MI, 48824-1321, USA*

[b]*Lawrence Livermore National Laboratory, Livermore, CA 94551-0808, USA.*

Abstract

We investigate two-proton correlation functions for sources that emit protons on two different time scales, one very short ($v \cdot \tau_{fast} \sim r_{source}$) and the other very long ($v \cdot \tau_{slow} >> r_{source}$). In such cases, the height of the correlation peak depends both on the source size and on relative yields from the slow and fast emission components. The width of the correlation peak, on the other hand, depends primarily on the source size of the fast component. The precise shape of the correlation function contains more detailed information, which can be quantitatively extracted by numerically inverting the correlation function. Such analyses confirm that precision two-proton intensity interferometry can disentangle slow equilibrium evaporation from fast preequilibrium emission.

PACS: 25.70.-z, 25.70.Pq

Intensity interferometry, the investigation of two-particle correlation functions at small relative momenta, can provide important information about the space-time characteristics and underlying dynamics of particle emitting sources [1-5]. At incident energies below the pion threshold, two-proton correlation functions have been the tool of choice for studying various equilibrium and non-equilibrium emission processes [4-19]. Initial analyses of two-proton correlation functions in terms of instantaneous emission from sources with Gaussian density profiles have yielded source radii that strongly depend on the energy of the emitted particles [8,11,12], indirectly signaling the importance of lifetime, expansion, and/or cooling effects. Later comparisons of measured correlation functions to predictions of reaction models, assuming either slow evaporative emission [10,14] or fast emission predicted by BUU transport calculations [11-13, 15-18], have provided more quantitative understanding. The correlation functions measured for intermediate-energy nucleus-nucleus collisions have been quantitatively reproduced by BUU transport calculations in a number of cases [11-13, 15]. Other data, primarily at higher incident energies [16-18], indicated emission time scales significantly longer than predicted by BUU transport theory. This led to speculations [18] that proton emission consists of two components involving radically different time scales -- a fast component consistent with BUU transport theory predictions and a slow component that might originate from the sequential decay of unstable nuclei produced in multifragmentation reactions [18].

In this paper, we investigate two-proton correlation functions that arise from such admixtures of fast and slow emission processes. Such scenarios may be rather common, with the fast component reflecting direct or preequilibrium emission and the slow component reflecting particle evaporation from equilibrated residues or sequential decays of particle-unbound primary fragments. We will show that in such cases the width of the correlation peak provides a clear measure of the source size for the fast component and that the height of the correlation peak provides the relative yields from the fast and slow emission components. We confirm these insights by a detailed re-analysis of the shapes of two-proton correlation functions that were measured previously for $^{14}N+^{197}Au$ collisions at E/A = 75 MeV [11] and were described rather unsatisfactorily by zero-lifetime Gaussian sources and by BUU calculations.

Experimentally, the (angle-integrated) two-proton correlation function 1+R(q) is defined in terms of the two-particle coincidence yield $Y_2(\mathbf{p}_1,\mathbf{p}_2)$ and the single particle yields $Y_1(\mathbf{p}_1)$ and $Y_1(\mathbf{p}_2)$:

$$\sum Y_2(\mathbf{p}_1,\mathbf{p}_2) = C\cdot\left(1+R(q)\right)\sum Y_1(\mathbf{p}_1)\cdot Y_1(\mathbf{p}_2). \qquad (1)$$

Here, $\mathbf{p}_1$ and $\mathbf{p}_2$ are the laboratory momenta of the two coincident particles, $q = \mu\cdot v_{rel}$ is the momentum of relative motion, and C is a normalization constant chosen such that $\langle R(q)\rangle = 0$ for large q where

final-state interaction effects are negligible. For a given experimental gating condition, the sums on each side of Eq. (1) extend over all particle energies and detector combinations corresponding to each bin of q.

Theoretical correlation functions are calculated from the angle-averaged Koonin-Pratt formula [1,3,9]

$$R(q) = 4\pi \int dr \cdot r^2 K(q,r) \cdot S(r), \qquad (2)$$

where the source function S(r) is defined as the probability distribution for emitting a pair of protons with relative distance r at the time the second proton is emitted. The angle-averaged kernel, K(q,r), is calculated from the radial part of the antisymmetrized two-proton relative wave-function. At short distances, K(q,r) is dominated by the strongly attractive singlet S-wave proton-proton interaction which gives rise to a maximum in R(q) at relative momentum $q \approx 20$ MeV/c. The long-range repulsive Coulomb interaction and antisymmetrization both produce a minimum at $q \approx 0$ MeV/c [1]. Both the peak at $q \approx 20$ MeV/c and the minimum at $q \approx 0$ MeV/c can be seen in the left hand panel of Fig. 1.

The peak at $q \approx 20$ MeV/c dominates the correlation functions for the fast emission component. Many analyses have assumed the source to be dominated by short time scale preequilibrium emission and have adopted a simple Gaussian profile,

$$S(r) = \frac{1}{(2\pi)^{3/2} r_0^3} \exp\left(-\frac{r^2}{2r_0^2}\right), \qquad (3)$$

where $\sqrt{3} \cdot r_0$ is the Gaussian rms two-proton source radius. For such Gaussian sources, the parameter r_0 describes the spatial distribution of emission points for zero lifetime sources [1,5] and is uniquely related to the height, R(20 MeV/c), (shown by the curve labeled as f = 1 in the lower right panel) and the width, Δq_{FWHM}, (shown in the top right panel) of the correlation peak.

In general, a non-zero emission timescale τ broadens S(r). For typical proton velocities v_{proton} such that $v_{proton} \cdot \tau$ is comparable to or larger than r_0, the complications of finite emission timescales need special consideration [1,5,9,10,13,14,19-21]. In the extreme limit of a very slow emission component, $v_{proton} \cdot \tau >> r_0$, for example, S(r) remains significant at large r where K(q,r) is dominated by the Coulomb interaction. The correlation function R(q) consequently vanishes except at very small relative momenta, $q < 20$ MeV where Coulomb and antisymmetrization effects are dominant [1]. Evaporation and other slow sequential decay processes therefore provide correlation functions that are small at most measured relative momenta and difficult to observe [21] in the presence of a strong fast

emission component. Nonetheless, the relative contributions of fast and slow emission components can be determined from a detailed shape of the correlation function using methods outlined below.

We illustrate the basis for separating fast and slow emissions via a schematic two-component model (STCM) in which the fast component is assumed to be instantaneously emitted ($\tau_1 = 0$) and the slow component is slow enough that its correlation function is negligible ($\tau_2 \approx \infty$). If fast emission provides a fraction, f, of the emitted protons, $Y_{1,fast} = f \cdot Y_1$, and if slow emission provides the remainder, $Y_{1,slow} = (1- f) \cdot Y_1$, the resulting correlation function R(q) is given by

$$R(q) = f^2 \cdot R_{fast}(q) \equiv \lambda \cdot R_{fast}(q) \ , \qquad (4)$$

where $R_{fast}(q)$ denotes the correlation function for fast emission only. Equation (4) stipulates that the height of the correlation function peak, R(20 MeV/c), is attenuated by the factor $\lambda = f^2$; thus, when fast and slow emission processes admix, the height of the correlation peak alone does not determine the source size. However the width of the correlation peak, Δq_{FWHM}, remains unaffected. This finding should remain approximately valid for more realistic emission time scales, $0 < \tau_{fast} << \tau_{slow} < \infty$, as long as $v_{proton} \cdot \tau_{slow} >> r_{source}$ while $v_{proton} \cdot \tau_{fast} \sim r_{source}$. However, the STCM becomes inaccurate in regions of relative momentum, where the long-lived component gives rise to a non-vanishing correlation function, $R_{slow}(q) \neq 0$. For time scales typical of particle evaporation or sequential decay, discrepancies must therefore be expected at very small relative momenta, q < 20 MeV/c [4,5,10,14], making the STCM unrealistic when emission is dominated by the slow component and the peak at $q \approx 20$ MeV/c is not strong.

For simplicity, we parameterize the fast emission component in the STCM according to Eqs. (3) & (4). The STCM thus contains two parameters, the Gaussian source radius r_0 and the fraction of coincident pairs resulting from the fast emission components, $\lambda = f^2$. Results obtained with the STCM are illustrated in Figure 1. The top right panel illustrates the unique relationship between Δq_{FWHM} and the radius of the fast source, r_0. The bottom right panel illustrates the dependence of R(20 MeV/c) on r_0 and f. The left panel shows how different combinations of f and r_0 can produce the same height of the correlation function peak, but not the same width.

The STCM indicates that accurate determinations of R(20 MeV/c) and Δq_{FWHM} should allow sensitive measures of the source size and the relative yields from fast and slow emission processes. Two-proton intensity interferometry may therefore provide a unique means to determine the relative strengths of equilibrium and preequilibrium emission components. (The argument above is readily

generalized to scenarios where fast and slow components are allowed to have different spatial dimensions. In such cases, Δq_{FWHM} determines the source size of the fast component.)

We apply these ideas to the interpretation of two-proton correlation functions measured at $\theta_{lab} \approx 25°$ for $^{14}N+^{197}Au$ collisions at E/A = 75 MeV [11]. The points in Figure 2 shows the correlation functions measured for proton pairs with three different cuts on their total momentum $P_{tot} = |\mathbf{p}_1+\mathbf{p}_2|$, 270 MeV/c < P_{tot} < 390 MeV/c (circular points), 450 MeV/c < P_{tot} < 780 MeV/c (triangular points), and 840 MeV/c < P_{tot} < 1230 MeV/c (square points). As observed for many other reactions [8,11,12,17,18], the height of the correlation peak increases with increasing P_{tot}. Correlation functions for zero-lifetime Gaussian sources are shown as dashed curves; the measured values of R(20 MeV/c) can be reproduced by using strongly momentum dependent radius parameters r_0 = 5.9 fm, 4.2 fm, and 3.4 fm, but the widths of the correlation function peaks cannot be reproduced by these calculations [11]. This inconsistency indicates that these strongly momentum-dependent radius parameters are meaningless.

As a first example, we show correlation functions calculated with the STCM that provide a good overall fit to the data (solid curves in Figure 2). For the three momentum bins (ordered by increasing values of P_{tot}), the extracted parameter sets are r_0 = 4.1±0.2 fm, f =0.5±0.1; r_0 = 3.3±0.1 fm, f = 0.7±0.1 and r_0 = 2.6±0.1 fm, f = 0.7±0.1. While these calculations provide a better description of the measured correlation functions than a simple Gaussian source, discrepancies remain -- especially in the fit to data at q>20 MeV/c for the lowest momentum cut 270 MeV/c < P_{tot} < 390 MeV/c. These discrepancies reflect the intrinsic limitation of the STCM noted above – the STCM becomes unrealistic at small relative momenta, q < 20 MeV/c, and when there is no clear maximum at q ≈ 20 MeV/c. Therefore, one cannot assert that the STCM provides a meaningful fit to the data at small relative momenta, q <20 MeV/c, and it may be more appropriate to fit the data only at q ≥ 20 MeV/c. Such fits, shown by the dot-dashed lines in Figure 3, yield the parameters r_0 = 1.7±0.4 fm, f =0.2±0.1; r_0 = 2.9±0.2 fm, f = 0.6±0.1 and r_0 = 2.5±0.1 fm, f = 0.7±0.1. The differences and similarities between the two parameter-sets illustrate the limitations of our schematic model. For the highest two cuts on P_{tot}, the peak of the correlation function peak is well determined and the extracted parameters are in reasonable agreement. Larger uncertainties exist for the lowest cut on P_{tot}. For this momentum cut, the correlations from slow emission cannot be neglected.

While different source geometries and more realistic parameterizations with finite lifetimes for both slow and fast emission components could be readily explored, we use the less model-dependent

approach of numerically inverting the correlation functions as described in refs. [22-24] to obtain more quantitative information. Following ref. [24], the sources were parameterized over $0 \leq r \leq 20$ fm by six third-order b-spline polynomials, and the numerical inversion of Eq. (2) was achieved via the optimization algorithm of ref. [23,24]. The thick gray curves in Figure 3 show the best fits to the experimental data with the imaging approach. The agreement with the experimental data is excellent.

The corresponding imaged sources are shown in Figure 4. The widths of these curves represent the lower and upper limits defined by one-sigma error bars of the extracted source functions. The uncertainties, small at $r<7$ fm, become very large at $r \geq 12$ fm. Better data in the small momentum region ($q < 10$ MeV/c) of the correlation functions could provide improved constraints on the source at large radii where the source shape is mainly determined by the time scale of the slow emission component. Unfortunately, this part of the correlation function is difficult to measure and the precision of the data at $q < 10$ MeV/c is limited, see, e.g., Figure 3.

Despite the restriction that one can only accurately image the source for $r \leq 12$ fm, the imaged sources directly reveal a two-component structure similar to that expected for emission with two very different time scales: the sharply localized central region can be attributed to a fast emission component, and the tail region can be attributed to a slow emission component. From the non-Gaussian sources obtained from the numerical inversion, we extract the half-density radii from the radial source profiles, $r_{1/2}$, and the yield ratio f from the central ($r < 3 \cdot r_{1/2}$) region of the imaged source distributions. The extracted quantities are given in Table I, where they are compared to the parameters extracted with the STCM (noting that $r_{1/2} \approx 1.18 \cdot r_0$ for Gaussian profiles). The source functions corresponding to the STCM fits over all q and for $q > 20$ MeV/c are shown by the solid and dot-dashed curves in Fig. 4, respectively.

All three analyses indicate a strong dependence of the preequilibrium fraction and a relatively weak dependence of the source radius on P_{tot}. Moreover, all three analyses agree very well for the highest momentum gate, where the numerical inversion procedure indicates that the preequilibrium source is nearly Gaussian. The discrepancies between the numerical inversion procedure and the two-component model fits for the lower total momentum gates occur because the corresponding sources are not Gaussian. There, the model independent numerical inversion procedure provides the more quantitative approach.

In summary, we have investigated the characteristics of angle-integrated two-proton correlation functions for scenarios in which protons are emitted on two very different time scales. An example of

such a scenario would be fast preequilibrium emission from the initial overlap of projectile and target and slow equilibrium evaporation or secondary decays of particle unstable fragments. When both fast and slow emissions are present, determination of the height and width of the correlation peak allow the extraction of the initial source geometry associated with the fast component and the relative yields from the slow and fast emission processes. Some additional information about the lifetime of the slow component might be extracted from future measurements of the detailed shape of the correlation function at very small relative momenta. Precision measurements of angle-integrated two-proton correlation functions may thus provide a valuable diagnostic tool for reactions where equilibrium and preequilibrium processes compete.

This work was supported by the National Science Foundation under Grant Nos. PHY-95-28844 and PHY-0070818. Part of this work was performed under the auspices of the U.S. Department of Energy by University of California, Lawrence Livermore National Laboratory under Contract W-7405-Eng-48.

References

1. S.E. Koonin, Phys. Lett. **B70**, 43 (1977).
2. M. A. Lisa et al., Phys. Rev. Lett. 84, 2798 (2000).
3. S. Pratt and M.B. Tsang, Phys. Rev. **C36**, 2390 (1987).
4. D.H. Boal, C.K. Gelbke, and B.K. Jennings, Rev. Mod. Phys. **62**, 553 (1990), and references therein.
5. W. Bauer, C.K. Gelbke, and S. Pratt, Ann. Rev. Nucl. Part. Sci, **42**, 77 (1992), and references therein.
6. S. Fritz et al., Physics Letters B, Vol. 461 (4) (1999) pp. 315.
7. H.A. Gustafsson, et al., Phys. Rev. Lett. 53, 544 (1984).
8. W.G. Lynch et al., Phys. Rev. Lett. **51,** 1850 (1983).
9. W.G. Gong et al., Phys. Rev. **C43**, 781 (1991).
10. W.G. Gong et al., Phys. Lett. **B246**, 21 (1990).
11. W.G. Gong et al., Phys. Rev. **C43**, 1804 (1991), and references therein.
12. M.A. Lisa et al., Phys. Rev. Lett. **70,** 3709 (1993).
13. M.A. Lisa et al., Phys. Rev. Lett. **71,** 2863 (1993).
14. M.A. Lisa, Phys. Rev. **C49**, 2788 (1994).
15. D.O. Handzy et al., Phys. Rev. **C51** (1995) 2237.
16. G.J. Kunde et al., Phys. Rev. Lett. **70** (1993) 2545.
17. S.J. Gaff et al., Phys. Rev. **C52,** 2782 (1995).
18. D.O. Handzy et al., Phys. Rev. Lett. **75,** 2916 (1995).
19. A. Elmaani et al., Phys. Rev. C49, 284 (1994).
20. C.J. Gelderloos et al., Phys. Rev. Lett. 75, 3082 (1995).
21. L. Martin et al., Nucl. Phys. A 583, C407 (1995).
22. D.A. Brown and P. Danielewicz, Phys. Lett. **B398**, 252 (1997).
23. D.A. Brown and P. Danielewicz, Phys. Rev. **C57**, 2474 (1998).
24. D.A. Brown and P. Danielewicz, nucl-th/0010108 (2000).

Table I: Values for the half radius $r_{1/2}$ and the fraction f of proton emission from the fast component that have been extracted following the procedures outlined in the text. The label STCM designates the fits using the schematic two-component model. (For the Gaussian profiles, $r_{1/2} \approx 1.18 \cdot r_0$.)

P_{tot} region	270 - 390 MeV/c		450 - 780 MeV/c		840 - 1230 MeV/c	
	$r_{1/2}$ (fm)	f	$r_{1/2}$ (fm)	f	$r_{1/2}$ (fm)	f
Numerical inversion	2.44±0.37	0.30±0.05	3.13±0.14	0.68±0.03	2.93±0.15	0.78±0.05
STCM: fit for q > 20 MeV/c	2.0±0.6	0.2±0.1	3.4±0.3	0.6±0.1	3.0±0.3	0.7±0.1
STCM: fit for all q	4.8±0.24	0.5±0.1	3.9±0.2	0.7±0.1	3.0±0.3	0.7±0.1

Figure Captions:

Figure 1: Two proton correlation functions predicted with the schematic two-component model (STCM) discussed in the text. The left panel gives examples of correlation functions with similar heights of the correlation peak, but different widths. The top right panel illustrates the unique relation between source size and width of the correlation peak; the line corresponds to a linear best fit to the points. The bottom right panel illustrates the relation between the height of the correlation peak, source radius and fraction of proton emission originated from fast processes.

Figure 2: Two-proton correlation functions measured [11] at $\theta_{lab} \approx 25°$ for $^{14}N+^{197}Au$ collisions at E/A = 75 MeV for three different cuts on the total momentum, $P_{tot} = |\mathbf{p}_1+\mathbf{p}_2|$, of the coincident protons pairs, 270 MeV/c < P_{tot} < 390 MeV/c (circular points), between 450 MeV/c < P_{tot} < 780 MeV/c (triangular points), and between 840 MeV/c < P_{tot} < 1230 MeV/c (square points). The dashed curves show theoretical correlation functions for instantaneous emission from Gaussian sources, with radius parameter r_0 adjusted to reproduce the height of the correlation peak. The solid curves show theoretical correlation functions fitted with the STCM over the full range of q.

Figure 3: The experimental data are the same as those in Figure 2. The thick grey lines show correlation functions predicted from sources reconstructed by the inversion technique of refs. [22-24]. The dot-dashed curves show theoretical correlation functions fitted with the STCM to the data at q > 20 MeV/c.

Figure 4: Sources reconstructed from the data (Fig. 3) via the inversion technique of refs. [22-24] are shown as bands. The widths of the bands indicate the experimental uncertainties. The sources corresponding to the STCM fits over all q and for q > 20 MeV/c are shown by the solid and dot-dashed curves in Fig. 4, respectively.

Figure 1

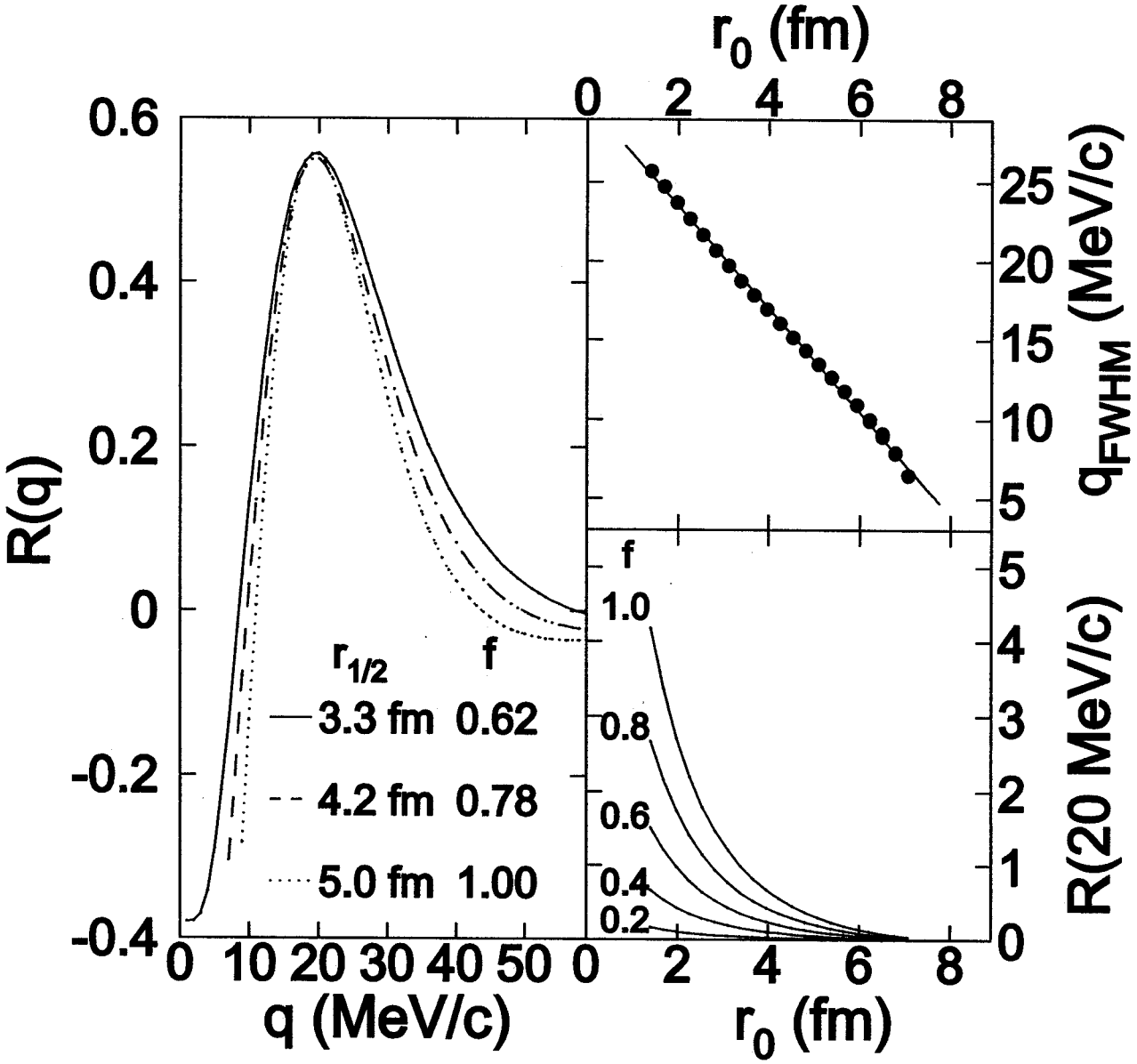
r0 (fm)
0 2 4 6 8
0.6
0.4
0.2
0
-0.2
-0.4
R(q)
0 10 20 30 40 50
q (MeV/c)
r1/2 f
3.3 fm 0.62
4.2 fm 0.78
5.0 fm 1.00
25
20
15
10
5
qFWHM (MeV/c)
f
1.0
0.8
0.6
0.4
0.2
5
4
3
2
1
0
R(20 MeV/c)
0 2 4 6 8
r0 (fm)

Figure 2

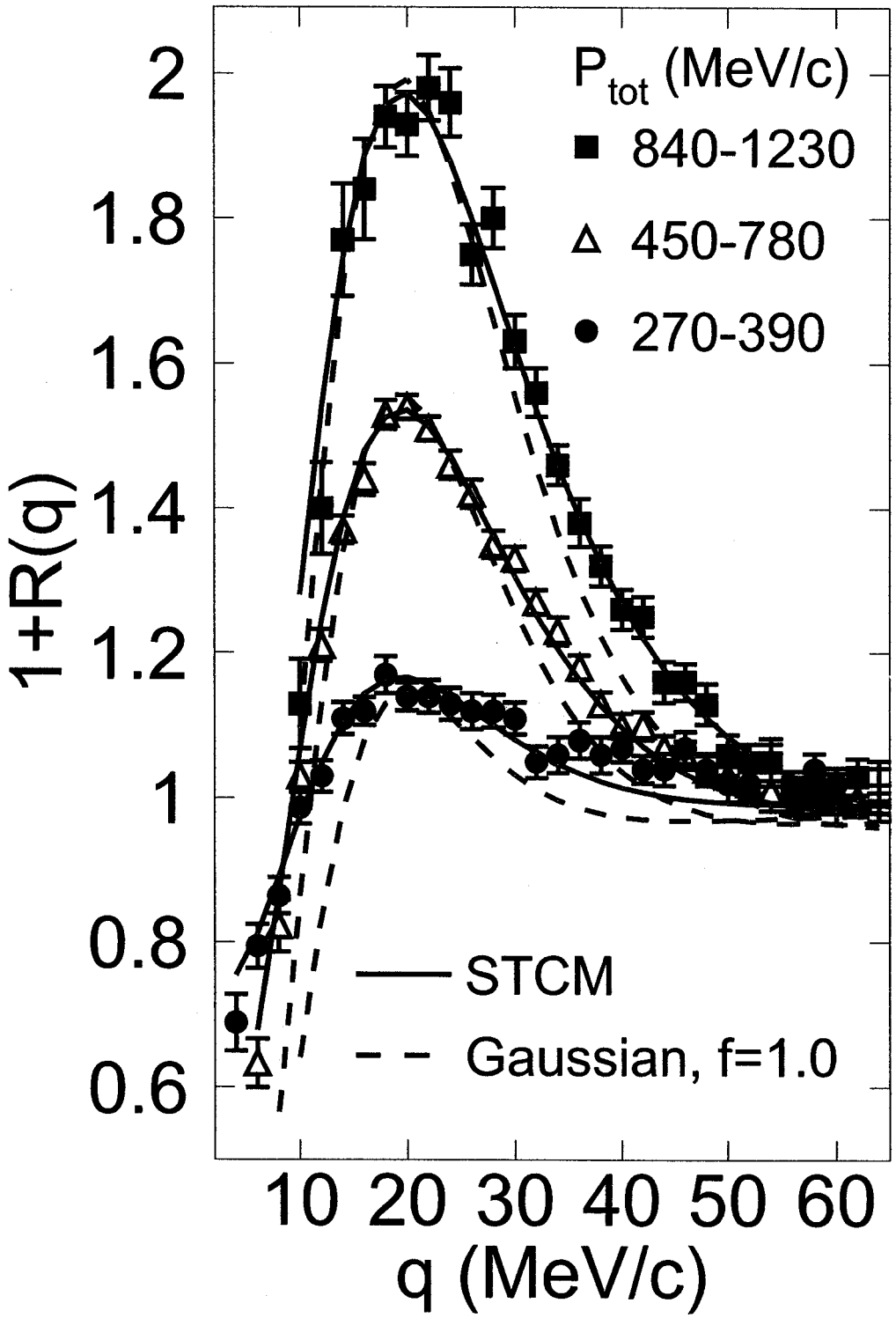
P_{tot} (MeV/c)
840-1230
450-780
270-390
STCM
Gaussian, f=1.0
1+R(q)
q (MeV/c)
2
1.8
1.6
1.4
1.2
1
0.8
0.6
10 20 30 40 50 60

Figure 3

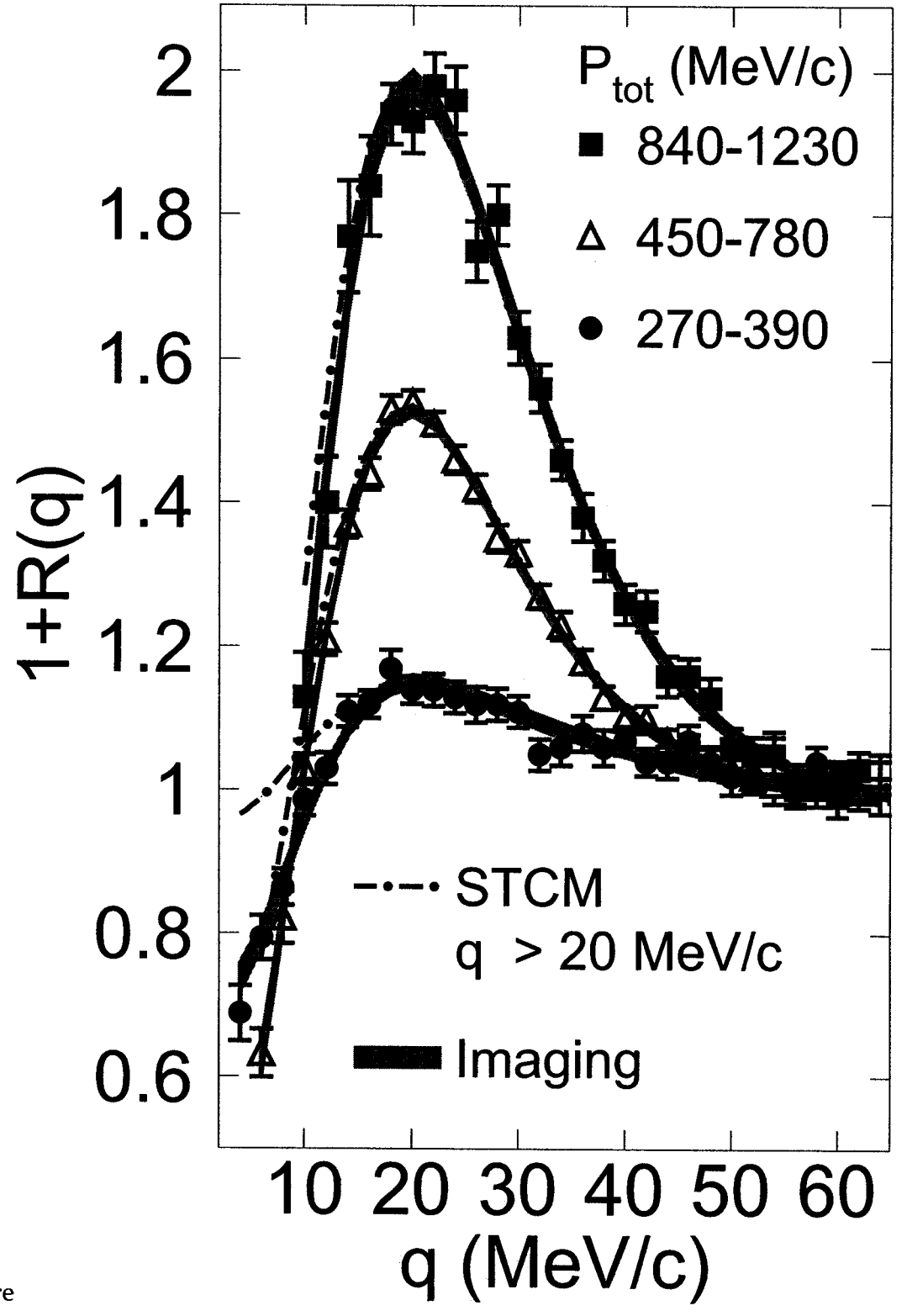

Figure

Figure 4

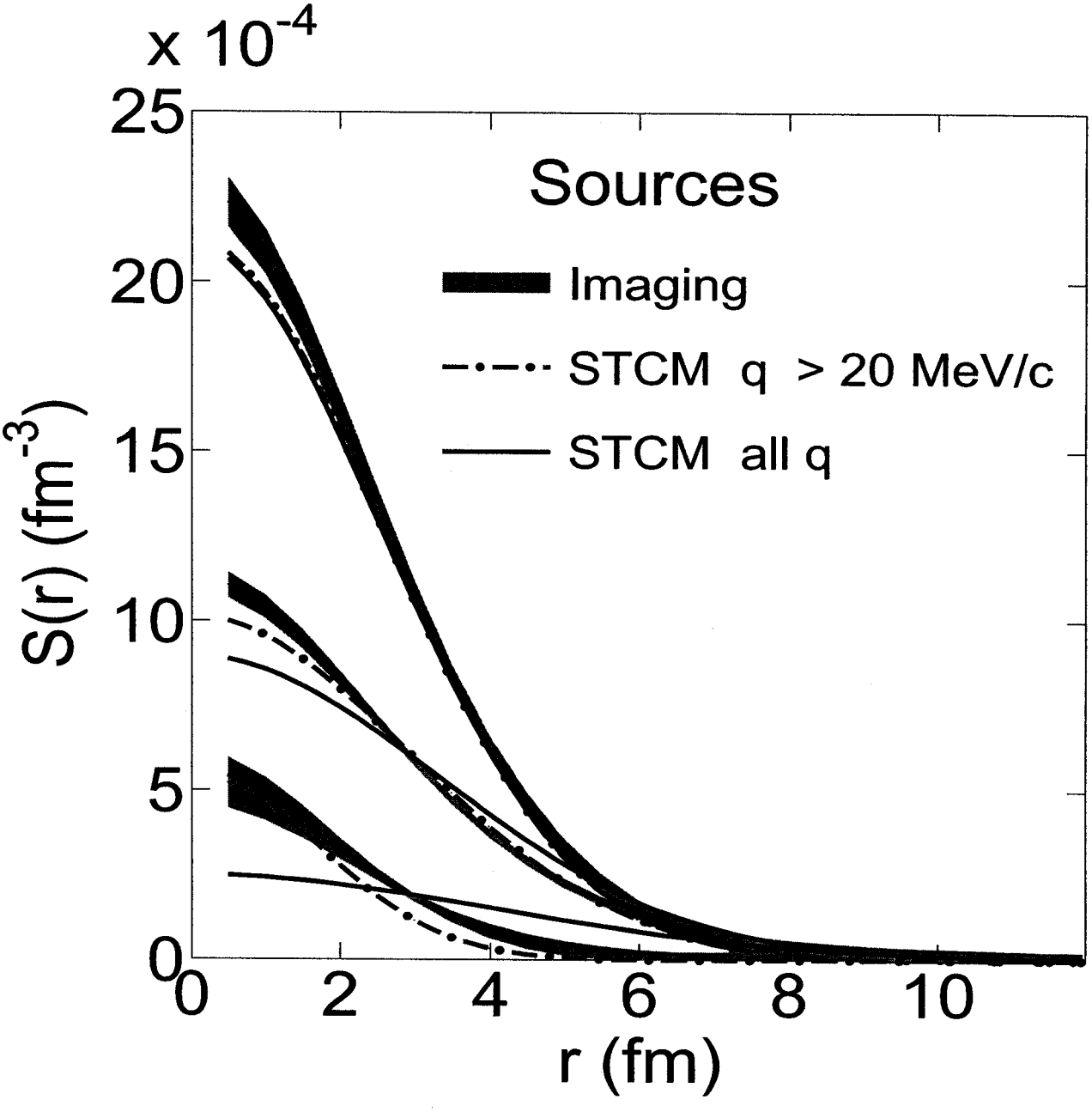
x 10^-4
25
20
15
10
5
0
S(r) (fm^-3)
Sources
Imaging
STCM q > 20 MeV/c
STCM all q
0
2
4
6
8
10
r (fm)